Hydroacoustic Constraints on the Rupture Duration, Length, and Speed of the Great Sumatra-Andaman Earthquake

Maya Tolstoy and DelWayne R. Bohnenstiehl
Lamont-Doherty Earth Observatory, Columbia University

INTRODUCTION

On 26 December 2004, one of the largest recorded earthquakes occurred, triggering a devastating tsunami that killed an estimated 300,000 people. The event was initially classified as M_w 9.0 based on the analysis of seismic body and surface waves (Nettles and Ekstrom, 2004; Ji, 2005; Park et al., 2005). Classical methods of magnitude calculation are hampered by the long duration of the event, however, since late-arriving phases from the earliest portion of the rupture may obscure first-arriving energy sourced from other portions of the rupture. This same phenomenon also limits our ability to constrain the earthquake's duration, length, and speed of propagation.

To work around these limitations, Stein and Okal (2005) studied Earth's low-order normal modes to estimate the size of the earthquake. Their results indicated a moment of 1.3 × 10^{30} dyne-cm (M_w 9.3), which is ~2.5 times larger than initial reports, and a centroid position near 7°N. In contrast with previous analyses, which had suggested displacement occurred primarily along the southern third of the aftershock region (Ji, 2005; Yagi, 2005; Yamanaka, 2005), these results argue that significant slip occurred along the entire aftershock zone.

For shallow submarine earthquakes, hydroacoustic recordings of tertiary (T) waves can provide additional constraints on rupture length, as well as velocity and direction of rupture propagation (e.g., Bohnenstiehl et al., 2004). T waves are formed when seismically generated energy is scattered at the seafloor-ocean interface and becomes trapped in the ocean's low-velocity wave guide, which is known as the SOund Fixing And Ranging (SOFAR) channel (Tolstoy and Ewing, 1950). Locating the source of a T wave, therefore, does not necessarily provide an estimate of the earthquake epicenter, but rather the position of the T-wave radiator. This is particularly true for the subduction zone environment (de Groot-Hedlin and Orcutt, 1999; Graeber and Piserchia, 2004), where long land paths may exist prior to acoustic conversion. In such instances, the T-wave radiator locations might vary with azimuth to a particular station, adding ambiguity to the locations derived from multiple stations. Great care should be taken in evaluating the influence of local bathymetric variations within the source region and considering whether a T-wave radiator location is representative of the earthquake's epicenter.

In part because of limitations relative to local three-component seismic data, T waves have not been widely exploited for earthquake studies, except in the case of midocean-ridge investigations (e.g., Fox et al., 1995; Fox et al., 2001; Smith et al., 2002), where local seismic data are very expensive to obtain. For remote portions of an ocean basin, a small number of hydrophones can improve the magnitude of completeness of a midocean-ridge earthquake catalog by more than one order of magnitude (Bohnenstiehl et al., 2002). T-wave data tend to play a complementary role to seismic data and often can yield tectonic and geological information that would not have been obtained using existing seismic networks.

The Indian Ocean is the site of three hydroacoustic stations operated as part of the International Monitoring System (IMS). These data are usually only available through national data centers of signatory countries to the Comprehensive Test Ban Treaty. Within the U.S., only organizations with active contracts to use the data, generally with the Air Force, have access. Because of the unusual global importance of this event, however, some data from the IMS have been made openly available for 26 December 2004 (http://www.rdss.info/).

At each Indian Ocean hydroacoustic station, three hydrophones are deployed in a triangular configuration with ~2 km spacing between sensors. These hydrophone triads are moored offshore of the Diego Garcia atoll, southwestern Australia, and Crozet Island. Our analysis is focused on signals recorded at the Diego Garcia South (DGS or H08S) triad (Figure 1), since this station provides the best azimuthal coverage, with minimally variable crustal paths, from the Sumatran-Andaman rupture zone. The frequency response of the hydrophone system is flat to within 3 dB over the range of 3–100 Hz.

HYDROACOUSTIC ANALYSIS AND METHODS

To identify T-wave radiator locations, azimuthal estimates are derived by inverting the differential travel times between sensors within the DGS hydrophone triad. Travel-time differ-
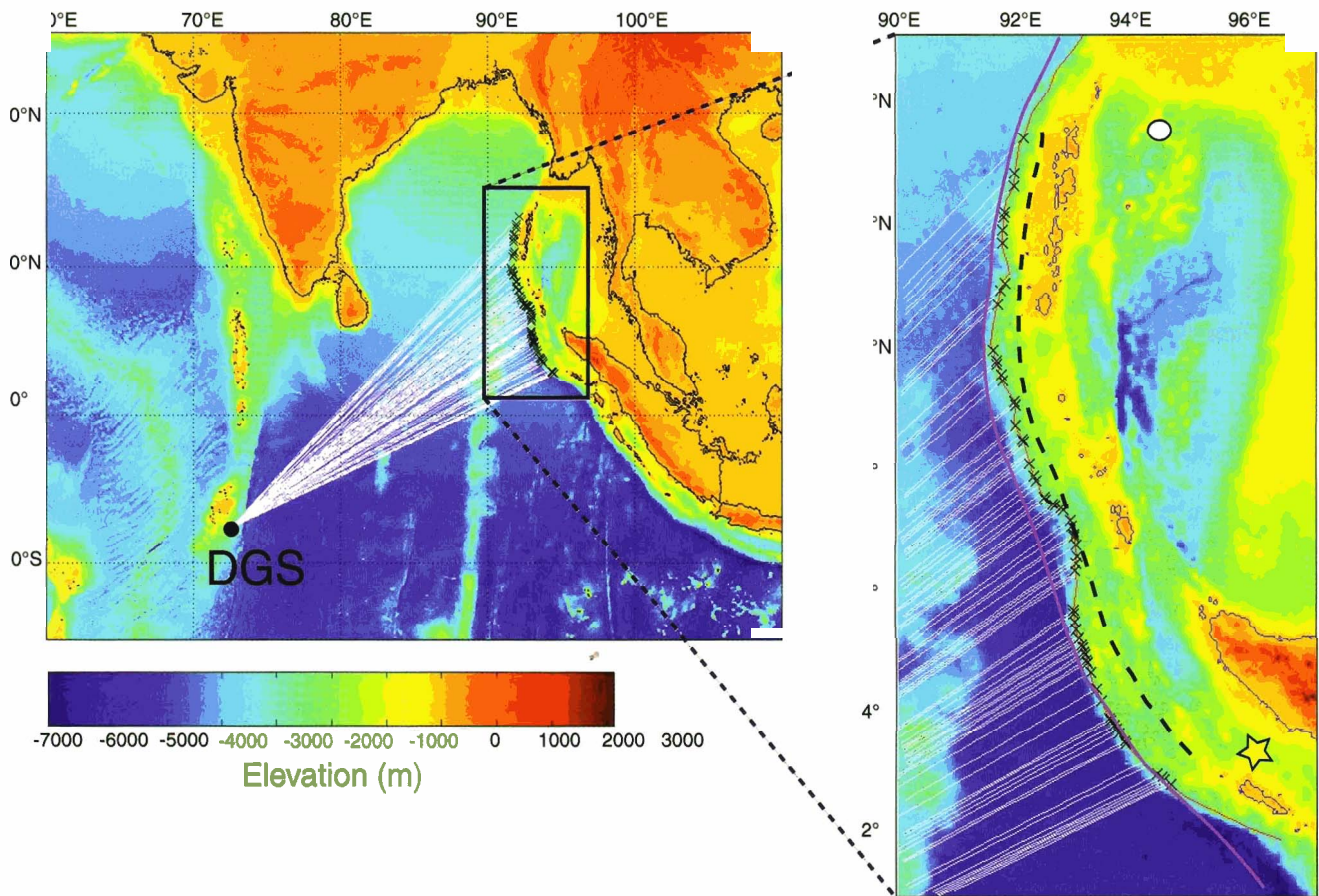
▲ **Figure 1.** Location of Diego García hydrophone triad with calculated azimuthal paths to the *T*-wave source region. Thin black lines indicate coastline. Close-up shows the *T*-wave radiator locations along the 2,000-m contour (red line) as black *X*'s, with the epicenter marked as a yellow star. The trace of the trench fault is shown as a purple line, and the thick dashed black line shows the track of the trench projected back onto the region directly behind the 2000-m contour. This track was used to correct arrival times for differential land paths. This enabled travel times to be projected back to a fault-parallel source, removing the effects of meandering bathymetry in distance and time calculations. White circle indicates the pole of rotation between the Indian Plate and Burma Plate (Bird, 2003). Azimuth traces from Diego García are visible on both maps.

ences between each pair of hydrophones ($t_{i,j}$) within the station's triad were derived from the cross-correlation of the 4–6 Hz band-passed signal arrivals, within 10-s windows having 50% overlap. These delay times were used in a plane wave-fitting inversion to determine the horizontal slowness components (p_x, p_y) and estimate the back-azimuth to the source region (*e.g.*, Del Pezzo and Giudicepietro, 2002). This relation between the time delay and horizontal slowness can be expressed as the dot product $\mathbf{t} = \mathbf{p} \cdot \mathbf{\Delta}$ and solved in a least-squared sense:

$$\mathbf{p} = \left(\mathbf{\Delta}^T\mathbf{\Delta}\right)^{-1}\mathbf{\Delta}^T\mathbf{t} \qquad (1)$$

where $\mathbf{\Delta}$ describes the geometric position of the hydrophone sensors. The velocity (v) and azimuth (α) are then given as $v = 1/|\mathbf{p}|$ and $\alpha = \tan^{-1}(p_x/p_y)$. As the sound velocity in the vicinity of the mid- to low-latitude arrays is well constrained, the slowness value returned by the inversion, along with the

correlation coefficient between instruments, can be used to assess the quality of the azimuthal estimates, with azimuthal accuracy on the order of a degree (Chapp *et al.*, 2005).

To associate these azimuths with *T*-wave radiator locations, they are projected along a geodetic path onto the bathymetry near the subduction zone. We use the 2,000-m contour as the projection point, which represents the approximate midslope position along the west-facing trench wall. The SOFAR velocity minimum in this area is at a depth of ~1,400 m, but energy is likely transmitted into the SOFAR channel over a broad range of depths. The *T*-wave radiation time was calculated by subtracting the predicted travel time of the hydroacoustic signal, assuming a velocity of 1.475 km/s, from the arrival time. Because the shelf wall contains significant meandering structures that do not relate to the fault, an additional correction is applied to adjust the source times to a common land path. Here we use a trench-parallel line constrained to intersect the 2,000-m contour at the point where the land path is minimized (Figure 1). A crustal *P*-wave velocity of 6 km/s is assumed in applying this correction.
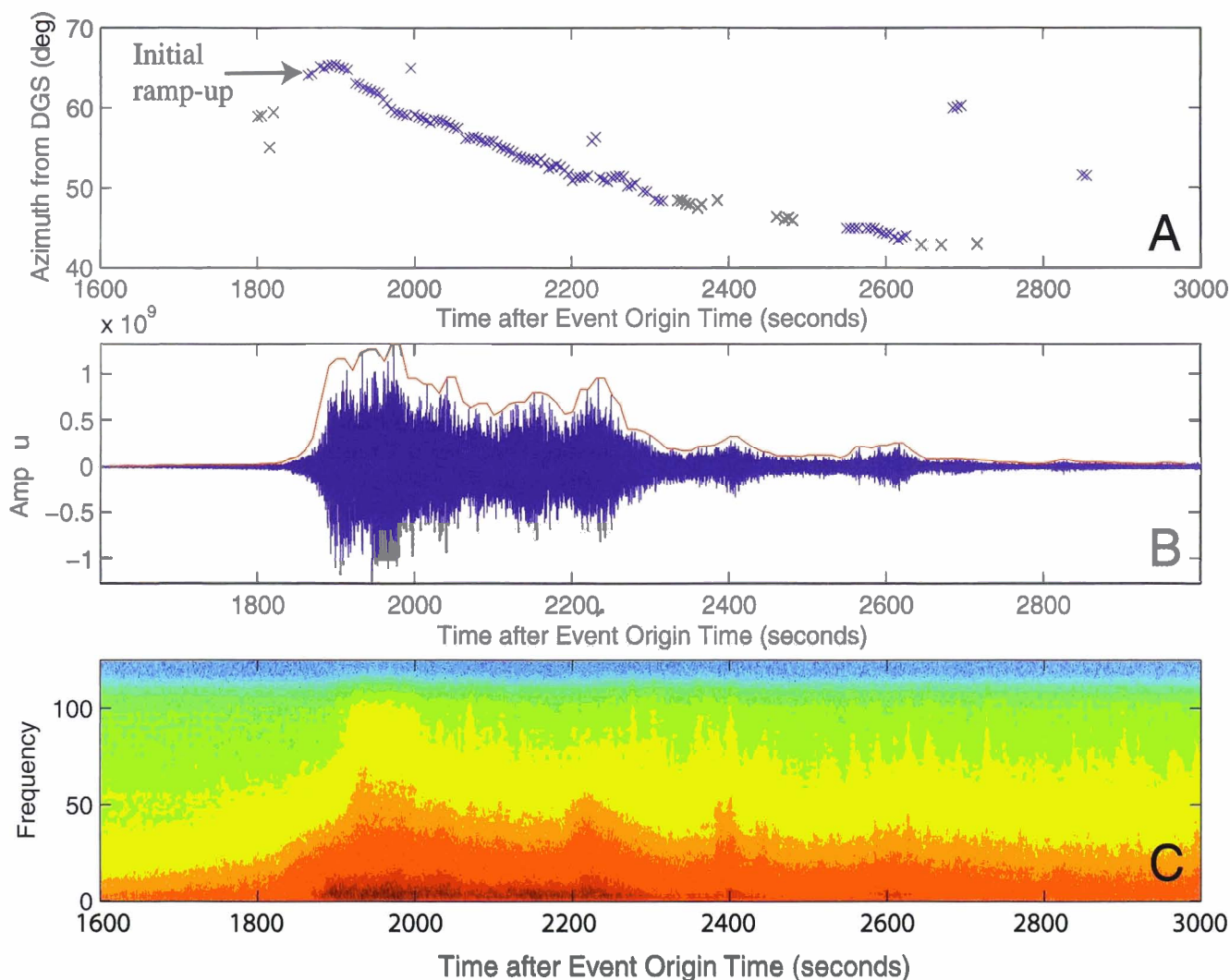
▲ **Figure 2.** (A) Calculated azimuth for waveform based on arrivals at three hydrophone channels at station DGS (H08S). (B) Waveform of *T*-wave arrival, with a 10-s envelope function shown in red. (C) Spectrogram of *T*-wave arrival illustrating the relative strength of different frequencies through time. Note that while the *T* wave itself lasts ~800 s, when the arrivals are corrected for difference in travel-time paths (Figure 1), the difference in source time of the first and last arrivals is ~480 s.

CONSTRAINTS ON RUPTURE DURATION, LENGTH, AND SPEED

Figure 2 shows the *T*-wave signal generated by the great Sumatra-Andaman earthquake, as recorded at the DGS station, along with its spectrogram and associated azimuth to the *T*-wave radiator. The southernmost azimuth (t = 1,900) associated with the initial large-amplitude arrival is within 0.4° of the epicenter location (3.3°N, 95.8°E), which lies ~165 km to the east-northeast from the trench wall (Figure 1). The azimuthal data show a northward trend (decreasing azimuth from DGS), as well as an initial small southerly trend associated with a gradual rise to the high-amplitude onset of the *T* wave (t = 1,865–1,900). This initial trend of arrival azimuths to the south represents energy sourced from the epicentral region but traveling on a less direct path. While this northerly path is longer, a greater proportion of it is spent

traveling as a *P* wave, because of the northwest trend of the shelf, resulting in earlier arrival at DGS. The low energy of the arrivals relative to the direct arrival is indicative of the less direct path (Graeber and Piserchia, 2004).

For these earliest arriving signals, the *T*-wave radiation time is estimated by subtracting the predicted acoustic travel time from the arrival time at DGS. Differencing the radiation time with the event's origin time provides an estimate of the crustal travel time and apparent crustal velocity. As the epicenter azimuth is approached (t = 1,900 s), apparent crustal velocity decreases, with the arrival most closely aligned with the epicentral azimuth exhibiting an apparent velocity of 2.8 km/s. This is a reasonable rupture velocity in this setting (Venkataraman and Kanamori, 2004) and consistent with the initial propagation of the rupture up-dip, as well as along-strike. Near-maximum peak amplitudes are reached as the rupture shallows (Figure 2), suggesting that the *T*-wave signal

may be dominated by seismic energy radiated from the shallowest portions of the rupture zone.

Figure 3A shows the cumulative distance along the rupture front, as estimated from the *T*-wave radiator positions (corrected for differential land paths), versus the source time. The slope of these points provides an estimate of the lateral rupture speed during the earthquake. A least-squares fit to the entire data set yields a mean velocity of 2.4 ± 0.2 km/s, consistent with the 2.5 km/s obtained by Ni *et al.* (2005) from the directivity of radiated high-frequency (2–4 Hz) seismic energy. The initial ~180 s of the rupture, however, is fit better by a velocity of ~2.8 ± 0.1 km/s, with the last ~300 s of the rupture characterized by a velocity of ~2.1 ± 0.2 km/s. This suggests a "two phase" rupture process.

To investigate the timing of this transition in rupture speed, the goodness of fit was evaluated for a series of best-fitting "two slope" models with the break points ranging from ~50–450 s (Figure 3B). The misfit between the predicted and observed positions of the rupture front (*T*-wave radiator location) is minimized for break points between 150–190 s, with a broader minimum between 150–290 s (Figure 3B). Across this range, least-squares velocity estimates are consistently higher for the first portion of the rupture (slope 1) relative to the second (slope 2), with the propagation speed slowing during roughly the second third of the rupture (Figure 3C).

Also constrained in Figure 3 are the duration of the rupture, ~480 s, and the total rupture length, ~1,200 km, similar to recent interpretations based on aftershock distribution (Stein and Okal, 2005) and high-frequency energy radiation (Ni *et al.*, 2005). This length and duration indicate the initial interpreted rupture length of only 400 km over 200 s led to underestimation of the magnitude, as proposed by Stein and Okal (2005). The rupture length of 1,200 km makes it the longest rupture ever recorded, ripping all the way from its epicenter near 3.3°N, 95.8°E to the end of the subduction zone at a latitude of ~13.5°N.

While the mainshock moment-tensor solution indicates thrust faulting, aftershocks show an increasing strike-slip component further north along the fault (Harvard Seismology, 2005; Kim, 2005). This is consistent with an increasingly oblique relative motion between the Indian and Burma Plates (Bird, 2003). The rupture terminates at the latitude of the pole of rotation (to within the error of the azimuth estimate) between these two plates, suggesting that the northern boundary of the subduction zone represents a tectonic barrier to rupture propagation, limiting the length and moment of this great earthquake.

Previous studies have suggested that many tsunamigenic subduction zone earthquakes contain slow-rupture components, which is manifested by low-radiation efficiency (Okal *et al.*, 2003; Venkataraman and Kanamori, 2004) and slow rupture velocity (Venkataraman and Kanamori, 2004). Such behavior has been linked to propagation through low-rigidity sediments within the accretion prism (Fukao, 1979) or heterogeneities along the subduction interface that lead to greater energy dissipation during rupture (Tanioka *et al.*, 1997; Polet and Kanamori, 2000). The later portion of the great Sumatra-Andaman earthquake is characterized by an average rupture velocity of 2.1 ± 0.2 km/s. This approaches the 1–2.0 km/s range cited for three tsunamigenic earthquakes in the global compilation of Venkataraman and Kanamori (2004).

Our observations indicate that high-frequency *T*-wave energy was radiated along the length of the rupture zone. The transition in rupture velocity occurs at a local minimum in the *T*-wave amplitude (Figure 4), which coincides spatially with a change in the trend of the aftershocks near 7°N (Stein and Okal, 2005). The occurrence of local amplitude maxima sourced from ~4–5°N and ~8–9°N are consistent with recent high-frequency radiation calculations (Ishii *et al.*, 2005) that indicate two peaks in energy released at ~80 s and ~320 s after onset. The later portion of the *T*-wave packet (sourced from north of ~9.5°N latitude) exhibits amplitudes that are roughly a factor of 4 lower than the earliest portion of the rupture (Figure 4). This may be consistent with lower radiation efficiency during the slower phase of rupture. Variability in the efficiency of *T*-wave coupling into the SOFAR channel, associated with changes in orientation of the trench wall, also may contribute to this pattern.

## IMPLICATIONS FOR EMERGENCY RESPONSE

When hydroacoustic data are available in near real-time, they may be used for rapid assessment of the spatial extents and moments of large submarine earthquakes. Such information could provide additional warning time for mobilizing rescue and relief efforts. It has long been postulated that *T* waves might be useful in predicting tsunamis (Ewing *et al.*, 1950), and recent work proposes a quantitative method for doing so (Okal *et al.*, 2003). Our results show that reliable early estimates of event size might be made simply by studying *T*-wave duration (Okal and Talandier, 1986) and projecting azimuthal information onto the bathymetry within the source region. This could be accomplished using a sparse network of small-aperture arrays, similar to those deployed as part of the IMS.

SUMMARY

T-wave azimuths and arrival times for the 26 December 2004 great Sumatra-Andaman earthquake measured by a hydrophone triad off the island of Diego García indicate a rupture duration of ~8 minutes and length of ~1,200 km. Rupture speed slows from 2.8 ± 0.1 to 2.1 ± 0.2 km/s after propagating ~450 km northward from the epicenter (3.3°N, 95.8°E). The latest arriving acoustic energy is sourced from the northern boundary of the India-Burma subduction zone at ~13.5°N latitude. Real-time analysis of hydroacoustic data may provide an effective method for rapidly evaluating the size and location of a large submarine earthquake. ▨
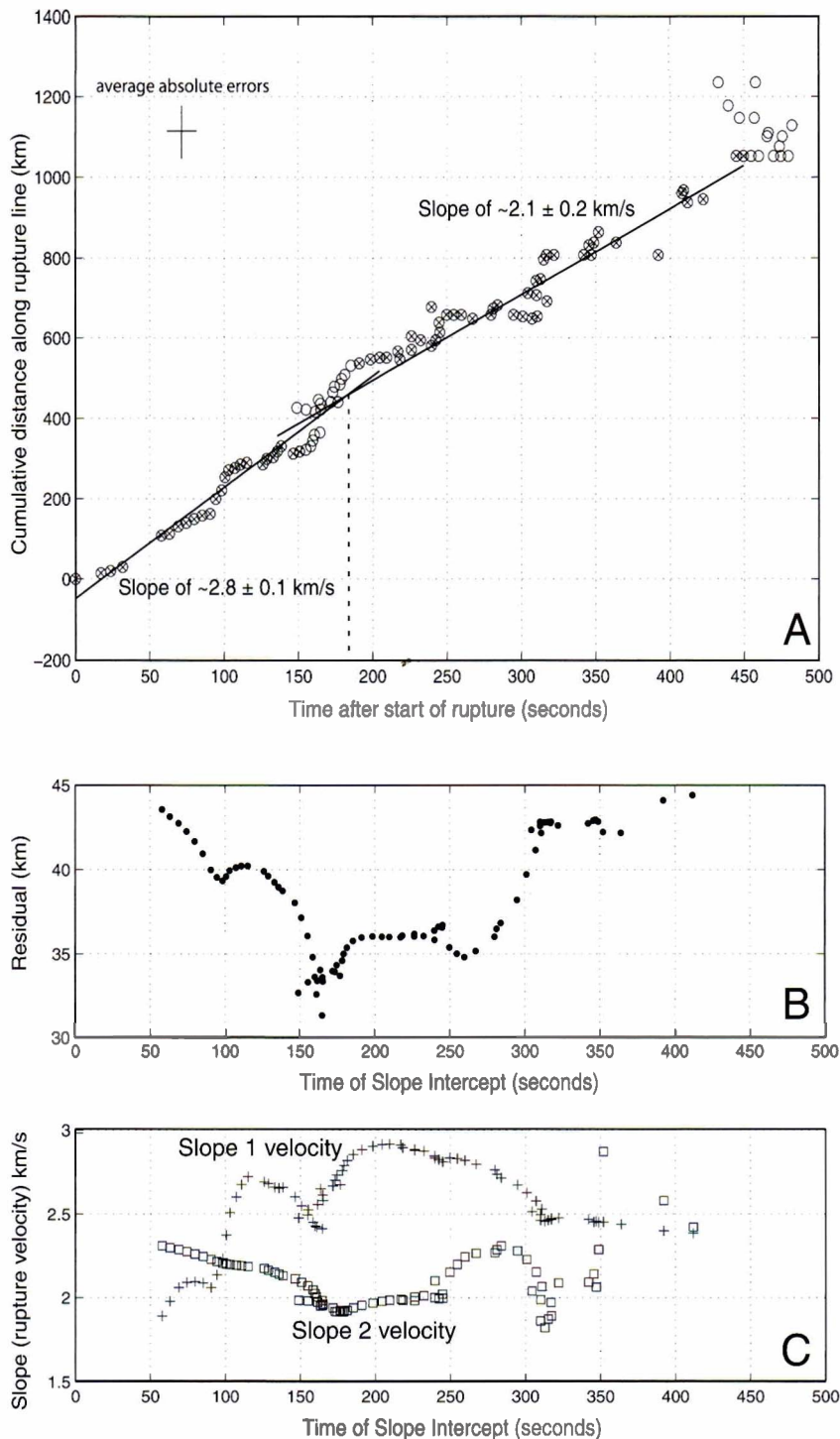
▲ Figure 3. (A) *T*-wave radiator locations are plotted as a function of cumulative distance along the rupture zone versus source time. Points marked with *x*s were used in determining the least-squares fit to these data (solid black). Points were excluded from the regression where complex bathymetry may influence the pattern of radiation (~150–190 s). Scatter from 450–480 s may be due to radiated energy coming from the area directly north of the rupture end. While the entire data set can be fit linearly with $R^2 = 0.976$ and a slope of 2.4 km/s, the early portion of the rupture is fit better by a slope of 2.8 ± 0.1 km/s, with $R^2 = 0.985$. A linear regression of the latter points yields a slope of 2.1 ± 0.2 km/s, with $R^2 = 0.953$. Average absolute errors (upper left corner) are shown based on a ±1° azimuthal accuracy and 10-s window used in the cross-correlation. Relative errors are likely to be significantly smaller. (B) Goodness of fit for a suite of two-slope models. Residuals represent the root-mean-square differences between the observed rupture front positions and the best fitting two-slope model for a given break point. Regressions included data with source times less than 450 s. The misfit is minimized for break points within the 150–190 s range, with a broader minimum between 150–290 s. (C) Velocity variations as a function of break-point position, with slopes 1 and 2 determined in a least-squares sense. Except for the more poorly fit models associated with the break points near the ends of the rupture, the velocity of slope 1 exceeds that of slope 2.
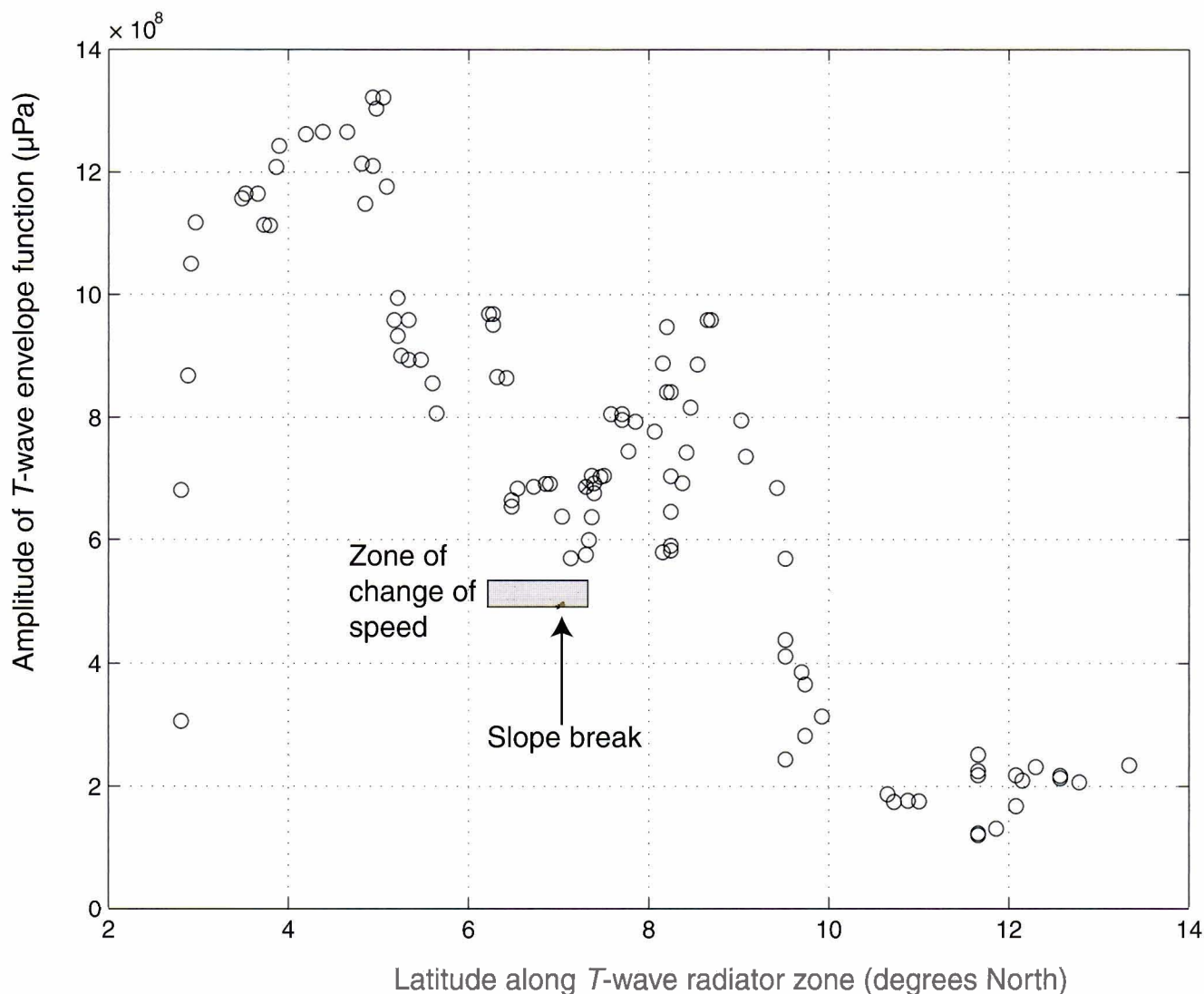
▲ **Figure 4.** Latitude along *T*-wave radiator zone versus amplitude of *T*-wave arrival based on the 10-s envelope function shown in Figure 2. The relative low in amplitude coincides with the transition in rupture rate visible in Figure 3. The gray box indicates the slope transition area from Figure 3 (150–190 seconds), and the arrow points to the slope break for the least-squares fit used, hence the location where the rupture velocity changes.

ACKNOWLEDGEMENTS

REFERENCES

Bird, P. (2003). An updated digital model of plate boundaries, *Geochemistry Geophysics Geosystems* **4**, doi:10.1029/2001GC000252.

Bohnenstiehl, D. R., M. Tolstoy, and E. Chapp (2004). Breaking into the plate: A 7.6 Mw fracture-zone earthquake adjacent to the Central Indian Ridge, *Geophysical Research Letters* **31**, L02615.

Bohnenstiehl, D. R., M. Tolstoy, D. K. Smith, C. G. Fox, and R. Dziak (2002). The decay rate of aftershock sequences in the mid-ocean ridge environment: An analysis using hydroacoustic data, *Tectonophysics* **354**, 49–70.

Chapp, E., D. R. Bohnenstiehl, and M. Tolstoy (2005). Sound-channel observations of ice-generated tremor in the Indian Ocean, *Geochemistry Geophysics Geosystems* (in press).

de Groot-Hedlin, C. D. and J. A. Orcutt (1999). Synthesis of earthquake-generated T waves, *Geophysical Research Letters* **26**, 1,227–1,230.

Del Pezzo, E. and F. Giudicepietro (2002). Plane wave fitting method for a plane, small, small aperture, short period seismic array: A MATHCAD program, *Computational Geoscience* **28**, 59–64.

Ewing, M., I. Tolstoy, and F. Press (1950). Proposed use of the T-phase in tsunami warning systems, *Bulletin of the Seismological Society of America* **40**, 53–58.

Fox, C. G., H. Matsumoto, and T. K. A. Lau (2001). Monitoring Pacific Ocean seismicity from an autonomous hydrophone array, *Journal of Geophysical Research* **106**, 4,183–4,206.

Fox, C. G., W. E. Radford, R. P. Dziak, T.-K. Lau, H. Matsumoto, and A. E. Schreiner (1995). Acoustic detection of a seafloor spreading

episode on the Juan de Fuca Ridge using military hydrophone arrays, *Geophysical Research Letters* **22**, 131–134.

Fukao, Y. (1979). Tsunami earthquake and subduction processes near deep sea trenches, *Journal of Geophysical Research* **84**, 2,303–2,314.

Graeber, F. M. and P. F. Piserchia (2004). Zones of T-wave excitation in the NE Indian Ocean mapped using variations in back azimuth over time obtained from multi-channel correlation of IMS hydrophone triplet data, *Geophysical Journal International* **158**, doi: 10.1111/j.1365-246X.2004.02301.x.

Harvard Seismology (2005). CMT Catalog Search, http://www.seismology.harvard.edu/CMTsearch.html.

Ishii, Miaki, Peter Shearer, Heidi Houston, and John E. Vidale (2005). Extent, duration and speed of the 2004 Sumatra-Andaman earthquake imaged by the Hi-Net array, *Nature*, doi:10.1038/nature03675.

Ji, Chen (2005). Magnitude 9.0 off the West Coast of Northern Sumatra, Preliminary Rupture Model, http://neic.usgs.gov/neis/eq_depot/2004/eq_041226/neic_slav_ff.html.

Kim, Won-Young (2005). Sumatra-Andaman Islands Earthquake, http://www.iris.iris.edu/sumatra/beachball_second.htm.

Nettles, Meredith and Goran Ekstrom (2004). Harvard Moment Tensor Solution, Magnitude 9.0 off the West Coast of Northern Sumatra, http://neic.usgs.gov/neis/eq_depot/2004/eq_041226/neic_slav_hrv.html.

Ni, S., H. Kanamori, and D. Helmberger, (2005). Energy radiation from the Sumatra earthquake, *Nature* **484**, 582.

Okal, E. A., P.-J. Alasset, O. Hyvernaud, and F. Schindelé (2003). The deficient T waves of tsunami earthquakes, *Geophysical Journal International* **152**, 416– 432.

Okal, E. A. and J. Talandier (1986). T-wave duration, magnitudes and seismic moment of an earthquake: Application of tsunami warning, *Journal of Physics of the Earth* **34**, 19–42.

Park, J., K. Anderson, R. Aster, R. Butler, T. Lay, and D. Simpson (2005). Global seismographic network records the great Sumatra-Andaman Earthquake, *Eos, Transactions of the American Geophysical Union* **86**, 57–64.

Polet, J. and H. Kanamori (2000). Shallow subduction zone earthquakes and their tsunamigenic potential, *Geophysical Journal International* **142**, 684–702.

Smith, D. K., M. Tolstoy, C. G. Fox, D. R. Bohnenstiehl, H. Matsumoto, and M. J. Fowler (2002). Hydroacoustic monitoring of seismicity at the slow spreading Mid-Atlantic Ridge, *Geophysical Research Letters*, doi:10.1029/2001GL013912.

Stein, S. and E. A. Okal (2005). Sumatra earthquake: Gigantic and slow, *Nature* **484**, 581–582.

Tanioka, Y., L. J. Ruff, and K. Satake (1997). What controls the lateral variation of large earthquake occurrence along the Japan trench?, *Island Arc* **6**, 261–266.

Tolstoy, I. and W. M. Ewing (1950). The T phase of shallow-focus earthquakes, *Bulletin of the Seismological Society of America* **40**, 25–51.

Yagi, Yuji (2005). Preliminary Results of Rupture Process for 2004 off Coast of Northern Sumatra Giant Earthquake (ver. 1), http://iisee.kenken.go.jp/staff/yagi/eq/Sumatra2004/Sumatra2004.html.

Yamanaka, Y. (2004). 04/12/26 off W. Coast of N. Sumatra, http://www.eri.u-tokyo.ac.jp/sanchu/Seismo_Note/2004/EIC161e.html.

Venkataraman, A. and H. Kanamori (2004). Observational constraints on the fracture energy of subduction zone earthquakes, *Journal of Geophysical Research* **109**, doi:10.1029/2003JB0025249.

Lamont-Doherty Earth Observatory
Columbia University
61 Route 9W
Palisades, NY 10964
tolstoy@ldeo.columbia.edu